AIAA JOURNAL
Vol. 36, No. 4, April 1998

Numerical Study of Supersonic Direct Current Plasma Nozzle Flow

Bertrand Jodoin,* Pierre Proulx,† and Yves Mercadier‡
Université de Sherbrooke, Sherbrooke, Québec J1K 2R1, Canada

To address the problem of studying the complex flow in dc supersonic plasma torches, an axisymmetric two-dimensional numerical code is developed. The aerodynamic fields are assumed to be expressed by a set of modified Euler equations in which heat conduction, generation, and radiative losses are included. A one-dimensional model is used for the nonequilibrium cathode sheath. The results for a 30-kW argon–hydrogen plasma are in good agreement with published experimental work. The theoretical results show that the structure of the flow can be divided radially in three distincts zones with specific transfer mechanisms, clarifying fundamental questions on this subject. The model results show significant improvement over simple engineering design methods for supersonic plasma jet nozzle.

Nomenclature

$\boldsymbol{E}$ = electric field, V/m
e = specific total internal energy, J/kg
I = current intensity, A
$\boldsymbol{J}$ = current density, A/m^2
J_r = radial current density, A/m^2
J_x = axial current density, A/m^2
k = thermal conductivity, W/m · K
n = normal direction
p = pressure, Pa
R = radiative losses, W/m^3
R_c = cathode radius, m
R_l = local radius of curvature, m
r = radial position, m
S = source term including radiative losses and Joule heating, W/m^3
T = temperature, K
t = time, s
u = axial velocity, m/s
u_t = tangential velocity, m/s
v = radial velocity, m/s
x = axial position, m
ρ = mass density, kg/m^3
σ = electrical conductivity, S/m
χ = electric potential, V

I. Introduction

THE low-pressure supersonic dc plasma jet is a technological tool that has found many applications in engineering. Plasma spray coating benefits from the reduced pressure, higher velocities, and longer heating zone that exist in the supersonic core of the plasma jet.[1,2] This configuration accelerates particles to higher impact speed, leading to a higher density of the deposit than usual coating processes and less contamination because it operates at reduced pressure. Ceramic coatings, ceramic–metals composite coatings, reactive coatings, formation of advanced-function intermetallic compound coating films, and surface modification are all successful examples of the application of this technology.[3] Figure 1 shows the cross section of a typical dc plasma torch.

For these applications, plasma characteristics in the nozzle strongly affect the system's performances. Thus, plasma diagnostic is significant for the material processing area. However, plasma features inside the nozzle are not well known because of the complex flowfields including the interaction between the arc, the cathode, and the gas flow. Although many experimental[4–7] and numerical[8–12] studies have been conducted, most of them were looking at the exit characteristics or neglecting the presence of the cathode leaving a gap in the complete picture of the system. Therefore, to this day, design of supersonic plasma nozzle has been based on quasi-one-dimensional theory or isentropic characteristics methods.

In an attempt to study the plasma characteristics inside the nozzle and develop a useful engineering tool for design, the present investigation was carried out. The approach used for this study is similar to those used in Refs. 13 and 14 for circuit breakers. It includes the cathode characteristics and interactions with the flow and electric field. The Euler equations, adding thermal conduction, radiative losses, and joule heating were obtained for an axisymmetric nozzle, along with the electric field. Finite difference simulations were conducted by applying Jameson's multistage method[15–17] for the aerodynamic fields and line-by-line Gauss–Seidel method for the electric field.[18] A simple one-dimensional model is used to represent the nonequilibrium behavior of the cathode sheath layer.

II. Model

A. Assumptions

1) There is local thermodynamic equilibrium (LTE). The assumption that the fluid is in LTE requires that collisional processes dominate over radiative processes and high elastic collision frequency, which is essentially the case in the bulk region of the plasma flow. Consequently, the plasma can be treated as a continuous fluid with one representative temperature. The population density follows Boltzmann distribution and Saha's law can be used to calculate the plasma composition. It is well known that the LTE assumption will fail near electrodes and in zones of high-temperature gradients. For this reason, a one-dimensional nonequilibrium model is used at the cathode sheath.

2) To close the aerodynamic equations system, the perfect gas law is used. This is generally a valid assumption for gas with low density, which is the case in this study.

3) Two-dimensional axisymmetric steady flow is assumed. This assumption simplifies the problem by reducing the number of grid points and the calculation time required to get a valid numerical solution. However, the physical phenomenon under study is three dimensional and unsteady so this assumption is a very restrictive one, far from the reality. The localized arc–anode attachment is one phenomenon exhibiting three-dimensional unsteady behavior. However, the fluctuations of the arc–anode attachment allow, on a time-average basis, the treatment of the aerodynamic fields as two-dimensional axisymmetric. Inasmuch as the two-dimensional axisymmetric assumption will be used, the arc–anode attachment cannot be localized because it would block the flow. To simulate the arc in two dimensions, a fictitious anode attachment is used.

Received June 18, 1997; revision received Nov. 24, 1997; accepted for publication Dec. 24, 1997.

*Applied Science Faculty, Department of Chemical Engineering.
†Vice-Dean of Research, Applied Science Faculty, Department of Chemical Engineering.
‡Professor, Applied Science Faculty, Department of Chemical Engineering.

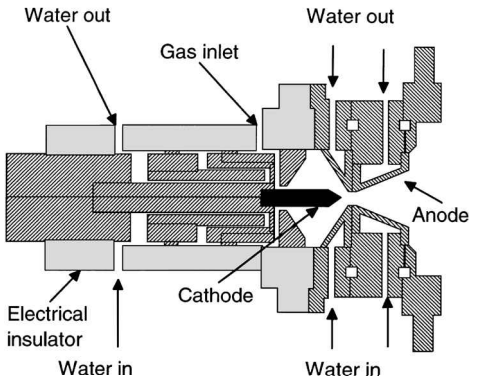

Fig. 1 Cross section of a dc plasma torch.

As found in Refs. 19 and 20, the anode attachment location does not change the general structure of the flow for subsonic flows. This numerical treatment will result in an error in the prediction of the voltage and to a higher arc length. Temperature fields may be overestimated as a result.

4) Radiation losses are given by the net emission coefficient method.

5) Lorenz forces are neglected. The electromagnetic forces will be neglected. It is expected that these forces will modify the flow near the tip of the cathode where current densities are high but this may in a first approximation be neglected because in supersonic flows the convective terms are very high.

6) Viscous effects are neglected. It is expected that the flow will be laminar in the major part of the flow, with a turbulent zone near the cold anode. For supersonic flows of this kind, the boundary layer is very small, and its effect on the flow will be minor inasmuch as the system presents a favorable pressure gradient. Therefore, the inviscid assumption will be used to reduce the calculation complexity and time.

These assumptions, especially the fictitious anode attachment, are expected to affect the results in such a way that the model may not exactly represent the physical situation, but it should properly represent the basic structure and behavior of the flow.

The proposed model is a combination of aerodynamic and plasma models for the flow and electrical model for the flow and the cathode with a sublayer model for the cathode sheath.

B. Aerodynamic and Plasma Models for the Flow

Based on the preceding assumptions, the continuity, momentum, and energy equations in their general conservative form can be expressed as follows:

$$\frac{\partial \boldsymbol{Q}}{\partial t}+\frac{\partial \boldsymbol{F}}{\partial x}+\frac{\partial \boldsymbol{G}}{\partial r}=\frac{\partial \boldsymbol{M}}{\partial x}+\frac{\partial \boldsymbol{N}}{\partial r}+\frac{\boldsymbol{D}}{r}+\boldsymbol{S} \tag{1}$$

with

$$\boldsymbol{Q}=\begin{bmatrix}\rho\\ \rho u\\ \rho v\\ \rho e\end{bmatrix},\qquad \boldsymbol{F}=\begin{bmatrix}\rho u\\ \rho u^2+p\\ \rho uv\\ \rho(e+p)u\end{bmatrix},\qquad \boldsymbol{G}=\begin{bmatrix}\rho v\\ \rho uv\\ \rho v^2+p\\ \rho(e+p)v\end{bmatrix}$$

$$\boldsymbol{M}=\begin{bmatrix}0\\ 0\\ 0\\ k\dfrac{\partial T}{\partial x}\end{bmatrix},\qquad \boldsymbol{N}=\begin{bmatrix}0\\ 0\\ 0\\ k\dfrac{\partial T}{\partial r}\end{bmatrix}$$

$$\boldsymbol{D}=\begin{bmatrix}-\rho v\\ -\rho uv\\ -\rho v^2\\ -(e+p)v+k\dfrac{\partial T}{\partial r}\end{bmatrix},\qquad \boldsymbol{S}=\begin{bmatrix}0\\ 0\\ 0\\ \dfrac{j_x^2+j_r^2}{\sigma}-R\end{bmatrix}$$

The perfect gas law is used to close this system with the Saha equilibrium relation for thermally ionized plasma gases.

C. Cathode Sheath Model

Immediately adjacent to the cathode surface the plasma is not in thermodynamic equilibrium. The one-dimensional nonequilibrium model proposed in Ref. 21 is used. This model takes into account the nonequilibrium effects in the cathode sheath region in an approximate way, assuming that the cathode is a thermoionic emitter. The charge continuity equation (which accounts for ambipolar diffusion, recombination, and ionization), a form of Ohm's law (relating the effective electrical conductivity with a local electric field), and the energy balance equation (accounting for thermal conduction, ohmic heating, plasma radiation, thermoionic cooling, ion heating, radiative heating from the plasma, and radiative cooling by thermal emission) are solved. The principal output of these calculations is the effective electrical conductivity of the electrode sheath that is then used to connect the sheath region with the cathode region and the flow region.

D. Electric Field Model for the Flow and Cathode (Excluding Cathode Sheath)

If the magnetic field is neglected, the Maxwell equations and Ohm's law, respectively, can be written for the steady-state electric field as follows:

$$\nabla\cdot\boldsymbol{J}=0 \tag{2}$$

$$\nabla\times\boldsymbol{E}=0 \tag{3}$$

$$\boldsymbol{J}=\sigma\boldsymbol{E} \tag{4}$$

The electric field can then be defined by a gradient vector of the electric potential χ, which yields

$$\nabla\cdot(\sigma\nabla\chi)=0 \tag{5}$$

III. Boundary Conditions

The boundary conditions are shown in Fig. 2.

A. Aerodynamic Fields

The boundary conditions introduced for the aerodynamic fields are as follows.

Assuming a subsonic inflow condition at the upstream boundary shown in Fig. 2 (B–C), characteristics analysis[18] indicates that three analytical boundary conditions can be specified; the other one, a numerical boundary condition, must be obtained by extrapolation of the interior solution. The temperature and pressure are specified and used to compute the density. The radial velocity is set equal to zero because parallel injection is assumed. The axial velocity is extrapolated from the interior solution by a second-order forward difference. The mass flow rate is, therefore, not given as an input but is a result of the model. Because a supersonic outflow condition is assumed at the nozzle exit [downstream boundary (E–D)], characteristics analysis dictates that all of the variables must be evaluated by extrapolation from the upstream region. It is done with second-order backward differences. The centerline boundary (E–F) is a line of symmetry with no mass and energy flux across it. The radial velocity component v is set equal to zero, whereas the symmetry condition is imposed by extrapolation on the other variables.

At the electrode boundaries (C–D and B–F), the slip condition is used. Magnitude of velocity vector is evaluated by extrapolations. The radial and axial velocity components are then determined. The gas temperature is specified at the anode surface. To calculate the pressure on the anode, a momentum balance is used, given by

$$\frac{\partial p}{\partial n}=-\rho\frac{u_t^2}{R_l} \tag{6}$$

The cathode initial temperature profile is based on the results of Ref. 22.

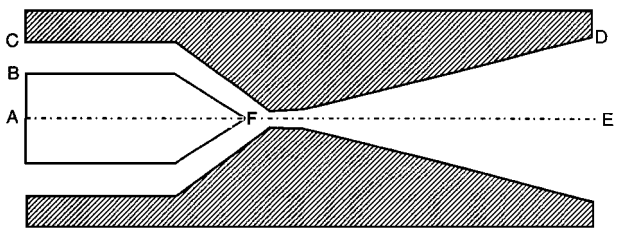

Fig. 2 Boundary conditions used in the calculations. A–B: J_x given by Eq. (7); B–C: $T=2000$ K, $P=1$ atm, $v=0$ m/s, and $J_x=0$ A/m^2; C–D: $T=2000$ K, slip condition, pressure given by Eq. (6), and voltage = 0 V; D–E: extrapolations and voltage = 0 V; and A–F–E: symmetry conditions.

B. Electric Field

For the electric field, the boundary conditions (Fig. 2) are as follows. The input current I is specified at the cathode boundary (A–B). Assuming that the current density j_x is uniform over this section the current density boundary condition is given by

$$j_x = I / \pi R_c^2 \tag{7}$$

The symmetry condition is imposed on the potential χ along the centerline boundary (A–F–E). The voltage is set to zero at the anode surface (C–D) and at the fictitious anode location (D–E). The current density j_x is set equal to zero at the open boundary (B–C).

IV. Numerical Aspects

A. Computational Grid System

To enhance the efficiency and accuracy of the numerical scheme and to simplify the implementation of boundary conditions, a transformation from physical space to computational space is performed. The domain of interest being simply connected, an elliptic grid generator is used, solving a Dirichlet problem of the Laplace equation. This method ensures that the mapping is one to one and that we have a smooth quasiorthogonal grid distribution with minimum skewness. The computational domain is a square divided into an equally spaced grid system. To solve the governing equations in the computational space, transformation of the equations from physical space into computational space is done.

B. Numerical Method and Procedure

Because the study involves a complex transonic flow in a simple geometry, a finite difference method is used. These methods have been used successfully for many years to study these kinds of problems.[23,24] The time-dependent aerodynamic fields are solved using Jameson's explicit scheme.

The electric field is computed in the steady form, separately from the aerodynamic fields because time intervals determined for these fields by Courant–Friedrichs–Lewy (CFL) values are generally large enough to regard the electric field in steady state. The electric field is discretized with a space-centered scheme, and the resulting algebraic set of equation is solved by using a line-by-line Gauss–Seidel scheme.[18]

The sequence of calculation is now described. As a first step, the isentropic quasi-one-dimensional flow is solved, given the temperature and pressure at the inlet. With this solution as an initial condition, the nozzle flow is calculated. The electric field is then computed, and the electric potential and discharge current density vectors and source terms are determined, followed by sheath calculations. Boundary temperatures at the plasma are then updated to ensure that energy balance is respected.[21] These calculations are repeated until the electric and aerodynamic fields are converged.

The model was validated for the case of a two-dimensional isentropic nozzle flow, based on the results of Ref. 25. The agreement was found to be excellent.

V. Results

A. Computational Details

A series of simulations was performed using an IBM Risc-6000/3AT workstation to study the sensitivity of the results to the grid used. We studied four different resolutions, with the resolution ranging from 60×20 to 80×30. The density contours obtained for the four cases are shown in Fig. 3. The flow features obtained with the coarsest grid (60×20) are not as well resolved as those using a finer grid. From Fig. 3, one can see that the 80×20 grid resolves all features of the flowfield, and so this grid will be used in the material presented subsequently. For the cathode sheath, 50 grid points were used.

The criterion for convergence used was based on the density residues expressed by

$$\sum_i \left(\rho_i^{n+1} - \rho_i^n\right) \Big/ \sum_i N_i \le 1 \times 10^{-9} \tag{8}$$

where $\sum_i N_i$ is the number of grid points.

The CFL number based on the average flow condition is 2.3 for the time step of 5 μs used for the computations. It took approximately 1.5×10^5 steps to converge to steady state with this CFL value.

Table 1 Comparison between experiment and calculations

Results	Flow rate, slpm	Voltage, V	Pressure, kPa	Temperature, K	Exit jet condition
Experiment	42	50	20	7900	Underexpanded
Calculations	42	57	25	7800	Matched pressure

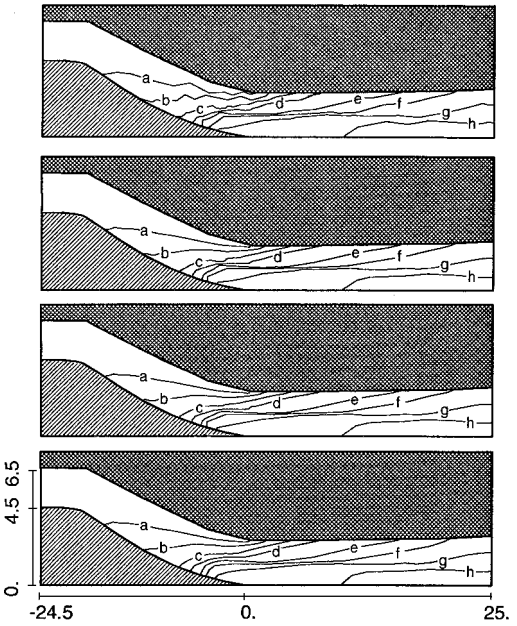

Fig. 3 Calculated mass density contours for the 600-A plasma; grid resolutions 60×20, 80×20, 100×20, and 80×30: a, 0.18 kg/m^3; b, 0.16 kg/m^3; c, 0.14 kg/m^3; d, 0.12 kg/m^3; e, 0.08 kg/m^3; f, 0.06 kg/m^3; g, 0.04 kg/m^3; and h, 0.02 kg/m^3.

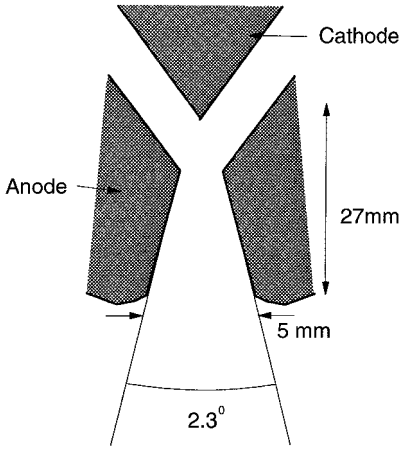

Fig. 4 Geometry of the nozzle of the torch.

B. Numerical Results

1. Validation

To further validate the numerical model under plasma conditions, calculations under the experimental conditions of Ref. 6 were done. The nozzle geometry is shown in Fig. 4. In the experiment, the throat diameter was 5 mm with a 2.3-deg divergent taper, and the gas used was a mixture of argon and hydrogen (17% H_2 by volume). The experimental input flow rates were 35 slpm (standard liter per minute) for argon and 7 slpm for hydrogen. The electric current was fixed at 600 A, for a cathode diameter of 9 mm.

All these parameters and conditions are used in the model except for the flow rate, which is an output of the model. Thermodynamic and transport properties used in the simulation for the argon–hydrogen plasma are taken from Murphy, and the details of their evaluation are described in Ref. 26. Linear interpolation is used for pressure lower than 100 kPa.

Table 1 shows a comparison between results from the experiment of Ref. 6 and the present calculations. The predicted mass flow rate

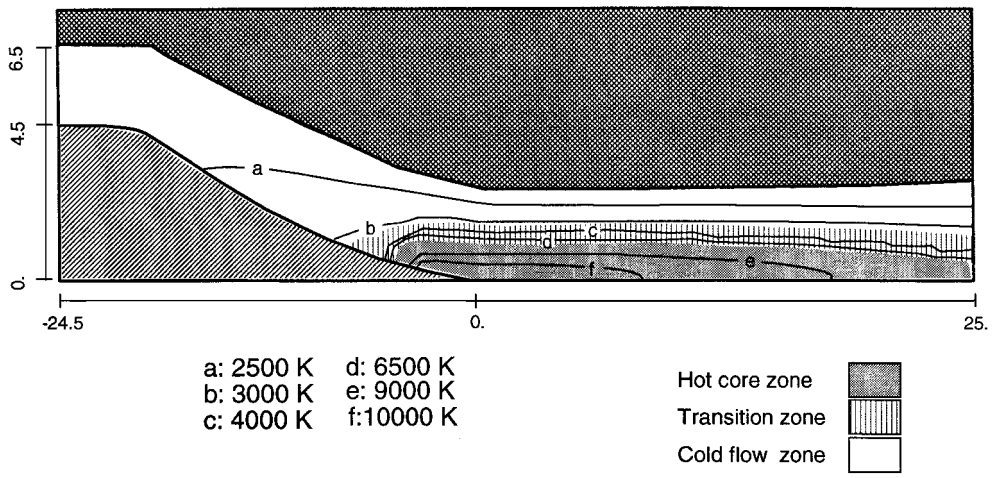

Fig. 5 Calculated temperature contours for the 600-A argon–hydrogen plasma.

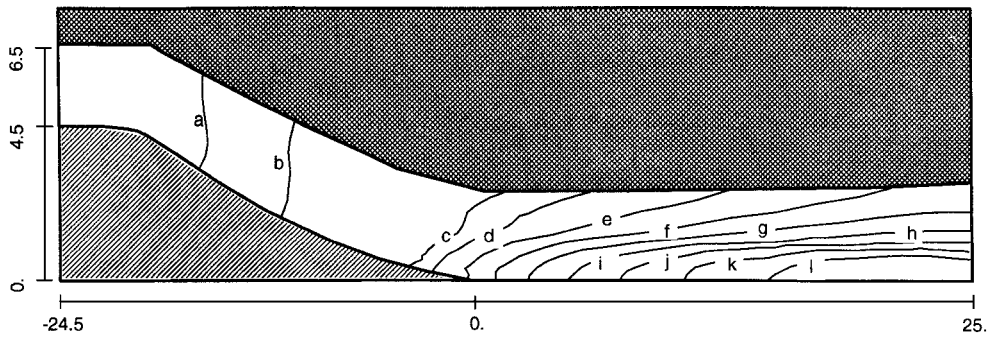

Fig. 6 Calculated velocity contours for the 600-A argon–hydrogen plasma: a, 100 m/s; b, 150 m/s; c, 450 m/s; d, 600 m/s; e, 800 m/s; f, 1000 m/s; g, 1200 m/s; h, 1400 m/s; i, 1600 m/s; j, 1800 m/s; k, 2000 m/s; and l, 2200 m/s.

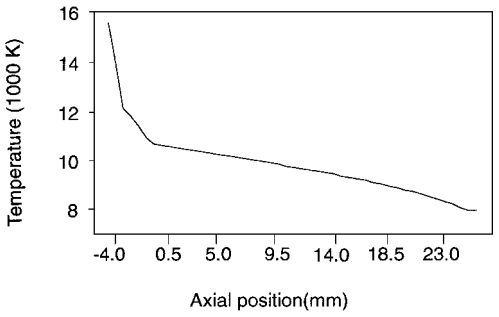

Fig. 7 Calculated temperature distribution at the symmetry line and near the cathode for the 600-A argon plasma (x = 0 throat location).

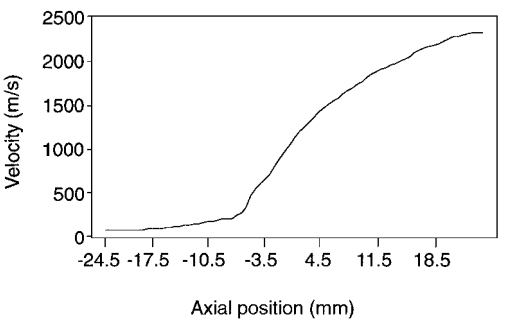

Fig. 8 Calculated axial velocity distribution at the symmetry line and near the cathode for the 600-A argon plasma (x = 0 throat location).

of the model is in agreement with the experimental value. The difference in the voltage could be explained by the use of a fictitious anode attachment. For the predicted exit pressure of 25 kPa, one can see that the experimental pressure of 20 kPa leads to an underexpanded plasma jet, as found by the experiment. The axis exit temperature is also in good agreement with the experiment.

2. Structure of the Flow

We now look at the structure of the flow for the test case conditions to improve the understanding of the mechanisms affecting the flow inside the nozzle. Figures 5 and 6 show the temperature and axial velocity contours, suggesting that the flow structure can be divided into three radial zones: the hot core zone, the transition zone, and the cold flow zone, as shown in Fig. 5. We now study each zone in detail.

1) The hot core zone is characterized by temperatures higher than 6000 K, and the gas can be considered as a plasma. This zone can be subdivided in two regions: the first one near the tip of the cathode, where the temperature is higher than 10,000 K, and the second one located after the first region, where the temperature is lower than 10,000 K. Figures 7 and 8 representing the temperature and axial velocity of the gas at the symmetry line and at the cathode show that near the tip of the cathode the axial temperature and velocity gradients ($\partial T/\partial x$ and $\partial u/\partial x$) are higher than in the second region. In the vicinity of the transition zone, radial temperature gradients ($\partial T/\partial y$) are also high. Table 2 summarizes these observations.

Figure 9 presents the mass density contours of the flow and shows that density is almost constant in the hot core zone. Pressure at the symmetry line and at the anode are shown in Fig. 10. One can observe that a high-pressure zone is built up at the tip of the cathode, as a result of the heating. This high pressure, combined with the effect of the geometry, leads to the acceleration of the gas at the tip of the cathode. After this region near the cathode tip, the pressure inside the hot core zone is matched with the pressure outside this zone and axial velocity gradients ($\partial u/\partial x$) are lower. It is, therefore, concluded that energy from the high-temperature zone at the tip of the cathode is transferred into kinetic energy, reducing the temperature of the plasma. Radiative heat transfer and conduction to the cathode also contribute to the temperature reduction.

Figures 11 and 12 show that temperature and axial velocity profiles are parabolic in the hot core zone. The flow is accelerated to supersonic velocity and is cooled down in the hot core zone as it progresses downstream.

2) The transition zone, or plasma boundary, is defined as the zone where the gas temperature drops from 6000 to 3500 K, the latter temperature being used to define the plasma radius. As shown in Table 2, radial thermal gradients ($\partial T/\partial y$) in this zone are very high. However, the velocity profiles, shown in Fig. 12, show no effect, as opposed to the large temperature gradients shown in Fig. 11. One can also notice from Fig. 9 the large mass density variation in this zone. These mass density and temperature variations are caused by the hydrogen recombination, which highly affects the local properties of the gas.

The plasma radius varies from 1.30 to 0.95 mm as the gas is cooled down by the surrounding cold fluid. One can, therefore, conclude that the transition zone acts as a buffer layer for the hot core zone. These high temperature gradients in the transition zone suggest that the chemical equilibrium hypothesis may be inappropriate in this zone.

3) In the cold flow zone, the temperature is lower than 3500 K and the gas is not in plasma state. The source terms from the arc are negligible, and the flow behaves as a classical compressible flow. The main effect of heating on this zone is to reduce the effective area and, therefore, to modify the geometry of the flow.

Figure 13 shows the calculated electrical potential. The voltage gradient is high near the cathode tip, where joule heating is dominant. Figure 14, presenting the calculated Mach number contours, shows the effects of heat addition to the flow and hydrogen recombination. Two distinct structures can be observed, one in the hot core zone and one in the cold flow zone. These structures are divided by the transition zone. In the hot core zone, the iso-Mach $M = 1$, which is usually located near the throat in regular compressible nozzle flows, is located at $x = 10$ mm. Figure 15 reveals that the iso-Mach profile is smoothed in the hot core zone. A small decrease

Table 2 Hot core zone characteristics

Characteristic	Near the cathode	In the divergent
T_{axis}, K	15,800–10,500	10,500–8,000
u_{axis}, m/s	200–1,100	1,100–2,300
$\partial T/\partial x$, K/m	$\sim 10^6$	$\sim 10^5$
$\partial T/\partial y$, K/m	$\sim 10^7$	$\sim 10^7$
$\partial u/\partial x$, m/s	$\sim 10^5$	$\sim 10^4$

Table 3 General characteristics of the argon–hydrogen flow

Characteristic	Value
Flow rate, slpm	42
Power, kW	35
Voltage, V	57
Exit pressure, kPa	25
T_{axis} (exit), K	7,800
u_{axis} (exit), m/s	2,300
T_{max}, K	15,800
Hot core radius (exit), mm	0.66
Plasma radius (exit), mm	0.95

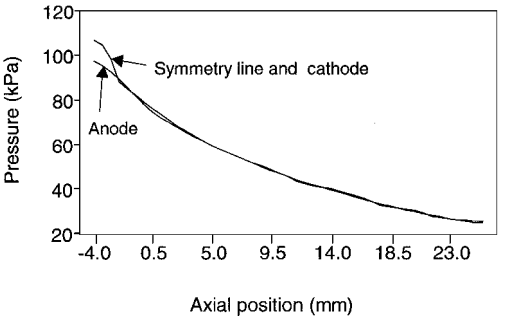

Fig. 10 Calculated pressure distribution at the symmetry line and near the cathode for the 600-A argon plasma ($x = 0$ throat location).

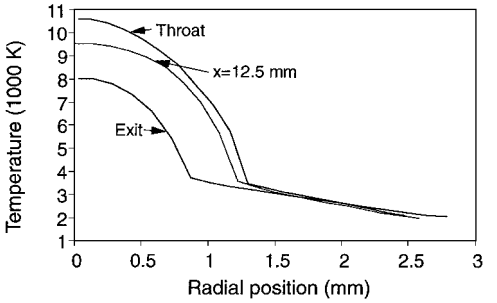

Fig. 11 Radial temperature profiles calculated at the throat, at $x = 12.5$ mm, and at the exit of the nozzle.

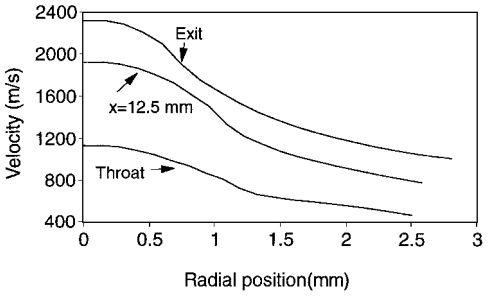

Fig. 12 Velocity profiles calculated at the throat, at $x = 12.5$ mm, and at the exit of the nozzle.

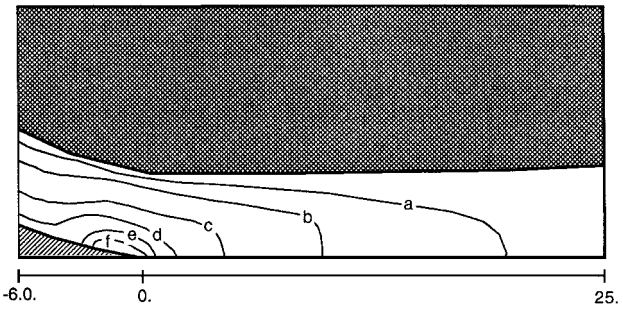

Fig. 13 Potential contours calculated for the 600-A argon–hydrogen plasma: a, − 5 V; b, − 15 V; c, − 25 V; d, − 35 V; e, − 45 V; and f, − 50 V.

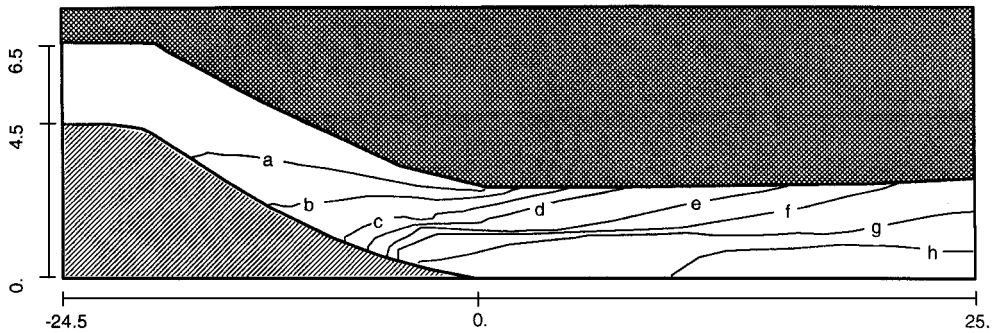

Fig. 9 Calculated mass density contours for the 600-A argon–hydrogen plasma: a, 0.18 kg/m^3; b, 0.16 kg/m^3; c, 0.14 kg/m^3; d, 0.12 kg/m^3; e, 0.08 kg/m^3; f, 0.06 kg/m^3; g, 0.04 kg/m^3; and h, 0.02 kg/m^3.

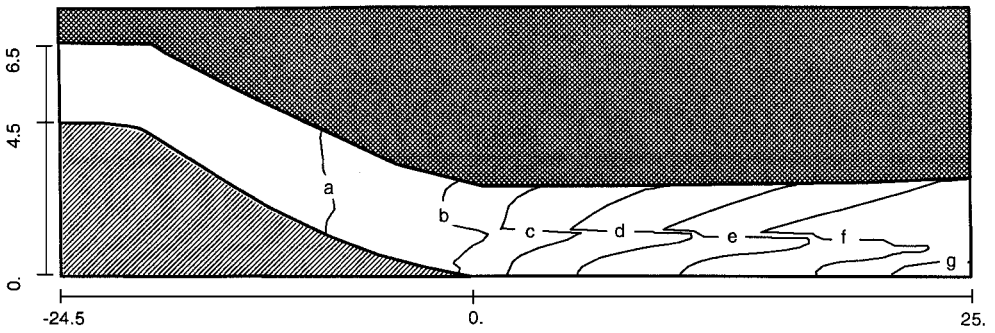

Fig. 14 Calculated Mach number contours for the 600-A argon–hydrogen plasma. a, 0.2; b, 0.4; c, 0.6; d, 0.8; e, 1.0; f, 1.2; and g, 1.3.

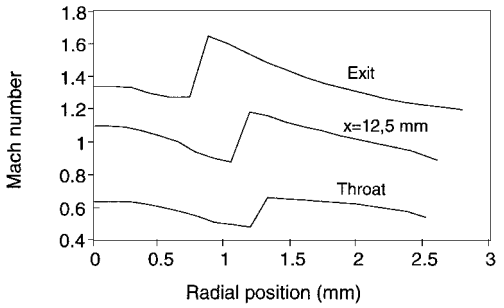

Fig. 15 Radial Mach number profiles calculated at the throat at, x = 12.5 mm, and at the exit of the nozzle.

of the Mach number is observable, resulting from the lower velocity with the radius.

In the cold zone, the iso-Machs have the same orientation as in the hot core zone. The iso-Mach $M = 1$ is also located downstream of the throat. One can conclude from this shift of location that the transition zone is heating the cold zone. From Fig. 14, one may conclude that using the Mach number contours is a good way to distinguish the three zones.

The quick change of the Mach number through the transition zone is due to the specific heat ratio of the argon–hydrogen mixture and the high temperature gradients in this zone.

By looking at the iso-Mach at the exit of the nozzle and considering that the value of the ratio of exit to throat diameters lead to exit Mach number of 1.8 (isentropic value), one can understand why the design of dc supersonic plasma torches based on the isentropic method is not efficient: The two-dimensional effects and the heat addition effects are important.

Table 3 summarizes the general characteristics of the argon–hydrogen flow, as calculated.

VI. Conclusion

The modified Euler equations and electric and cathode sheath equations have been solved using a finite difference method and coordinates transformation to investigate the flow characteristics inside a dc plasma torch. The method of solution has a very simple algorithmic structure, thus making it easily adaptable to geometrically complex flow with relative ease. The model agrees with available experimental results for a 30-kW argon–hydrogen plasma and clarifies certain aspects of the structure of the flow. It accurately predicts the underexpanded behavior demonstrated experimentally. The model shows the presence of a complex flow structure with three distinct zones. It can be used in conjunction with carefully planned experiments to improve the efficiency of supersonic dc plasma torches.

Acknowledgments

The authors wish to acknowledge the financial support of the National Sciences and Engineering Research Council of Canada. A. B. Murphy of the CSIRO, Australia, is gratefully acknowledged for providing the thermodynamic and transport properties used in the simulation for the argon–hydrogen plasma.

References

[1]Henne, R., Borck, V., Siebold, D., Mayr, W., Reusch, A., Rahmane, M., Soucy, G., and Boulos, M. I., "Converging–Diverging Nozzles for Improved Atmospheric Plasma Spraying," *Proceedings of 3rd European Conference on Thermal Plasma Processing*, VDI Berichte, Aachen, Germany, 1995, pp. 247–267.

[2]Rahmane, M., Soucy, G., Boulos, M. I., and Henne, R., "Diagnostics of D.C. Plasma Jets Generated with Laval Anodes," *Proceedings of the 1995 National Thermal Spray Conference* (Houston, TX), Vol. 1, ASM International, Materials Park, OH, 1995, pp. 157–162.

[3]Tahara, H., Uda, N., and Onoe, K.-I., "Discharge Features in a Steady-State Nitrogen Arcjet Engine with an Expansion Nozzle," *IEEE Transactions on Plasma Science*, Vol. 22, No. 1, 1994, pp. 58–64.

[4]Snyder, S. C., Lassahn, G. D., and Reynolds, L. D., "Direct Measurement of Gas Temperature and Gas Velocity Profiles in Sonic and Supersonic Argon–Helium Plasma Jets," *Proceedings of 11th International Symposium on Plasma Chemistry and Plasma Processing*, Vol. 1, International Organising Committee of 11th International Symposium on Plasma Chemistry, Loughborough, England, UK, 1993, pp. 386–391.

[5]Fincke, J. R., Swank, W. D., Snyder, S. C., and Haggard, D. C., "Enthalpy Probe Performance in Compressible Thermal Plasma Jets," *Review of Scientific Instruments*, Vol. 64, No. 12, 1993, pp. 3585–3593.

[6]Sabsabi, M., Vacquié, S., Gravelle, D. V., and Boulos, M. I., "Emission Spectroscopic Study of a Low Pressure Supersonic Ar–H_2 DC Plasma Jet," *Journal of Physics D: Applied Physics*, Vol. 25, No. 3, 1992, pp. 425–429.

[7]Cao, M., Sabsabi, M., Gravelle, D. V., Gitzhofer, F., Borck, V., and Boulos, M. I., "Effect of Nozzle Design on the Temperature Fields and the Spraying Characteristics of a Low Pressure D.C. Plasma Jet," *Proceedings of 11th International Symposium on Plasma Chemistry and Plasma Processing*, Vol. 1, International Organising Committee of 11th International Symposium on Plasma Chemistry, Loughborough, England, UK, 1993, pp. 162–167.

[8]Lee, Y. C., Hsu, K. C., and Pfender, E., "Modeling of Particles Injected into a D.C. Plasma Jet," *Proceedings from 5th International Symposium on Plasma Chemistry*, Vol. 1, International Union of Pure and Applied Chemistry, Edinburgh, Scotland, UK, 1981, pp. 795–803.

[9]Bourdin, E., Vardelle, A., Vardelle, M., Boulos, M. I., and Fauchais, P., "Computer Modelisation of Heat and Momentum Transfer Between a Particle and a D.C. Plasma Jet," *Proceedings from 5th International Symposium on Plasma Chemistry*, Vol. 1, International Union of Pure and Applied Chemistry, Edinburgh, Scotland, UK, 1981, pp. 804–811.

[10]Chang, C. H., and Ramshaw, J. D., "Modeling of Nonequilibrium Effects in a High-Velocity Nitrogen–Hydrogen Plasma Jet," *Plasma Chemistry and Plasma Processing*, Vol. 16, No. 1, 1996, pp. 5s–17s.

[11]Fang, M. T. C., Zhuang, Q., and Shen, M. Y., "The Computation of Axisymmetric Supersonic Nozzle Arc Using Adaptive Grids," *IEEE Transactions on Plasma Science*, Vol. 22, No. 3, 1994, pp. 228–234.

[12]Fang, M. T. C., Kwan, S., and Hall, W., "Arc-Shock Interaction Inside Supersonic Nozzle," *IEEE Transactions on Plasma Science*, Vol. 24, No. 1, 1996, pp. 85, 86.

[13]Vergne, P. J., "Simulation Numérique d'un Arc de Disjoncteur à Hexafluorure de Souffre en Présence d'un Écoulement Turbulent en Régime Stationnaire," Ph.D. Thesis, Laboratoire de Décharge dans les Gaz, Université Paul-Sabattier de Toulouse, Toulouse, France, March 1995.

[14]Zhang, X. D., Trépanier, J.-Y., and Camarero, R., "Computation of a Convection Stabilized 1200-A Arc in a Convergent–Divergent Nozzle," AIAA Paper 94-0693, Jan. 1994.

[15]Hirsch, C., *Numerical Computation of Internal and External Flows*, Vol. 2, Wiley, New York, 1990, pp. 334–339.

[16]Jameson, A., and Yoon, S., "Multigrid Solution of the Euler Equations Using Implicit Scheme," *AIAA Journal*, Vol. 24, No. 11, 1986, pp. 1737–1743.

[17]Jameson, A., "The Evolution of Computational Methods in Aerodynamics," *Transactions of the American Society of Mechanical Engineers*, Vol. 50, No. 4b, 1983, pp. 1052–1073.

[18]Hoffmann, K. A., *Computational Fluid Dynamics for Engineers*, Engineering Education System, Houston, TX, 1989, pp. 145–147.

[19]Bauchire, J. M., Gonzalez, J. J., and Gleizes, A., "Modeling of a DC Plasma Torch in Laminar and Turbulent Flow," *Plasma Chemistry and Plasma Processing*, Vol. 17, No. 4, 1997, pp. 409–432.

[20]Paik, S., Huang, P. C., Heberlein, J., and Pfender, E., "Determination of the Arc-Root Position in a DC Plasma Torch," *Plasma Chemistry and Plasma Processing*, Vol. 13, No. 3, 1993, pp. 379–397.

[21]Morrow, R., and Lowke, J. J., "A One-Dimensional Theory for the Electrode Sheaths of Electric Arcs," *Journal of Physics D: Applied Physics*, Vol. 26, 1993, pp. 634–642.

[22]Zhou, X., Ding, B., and Heberlein, J., "Temperature Measurement and Metallurgical Study of Cathodes in DC Arcs," *Proceedings of the 41st IEEE Holm Conference on Electrical Contact*, Vol. 1, Inst. of Electrical and Electronics Engineers, New York, 1995, pp. 219–223.

[23]Hasen, G. A., "Navier–Stokes Solutions for an Axisymmetric Nozzle," *AIAA Journal*, Vol. 20, No. 9, 1982, pp. 1219–1226.

[24]Chang, I.-S., "One- and Two-Phase Nozzle Flows," *AIAA Journal*, Vol. 18, No. 12, 1980, pp. 1455–1461.

[25]Kliegel, J. R., and Quan, V., "Convergent–Divergent Nozzle Flows," *AIAA Journal*, Vol. 6, No. 9, 1968, pp. 1728–1734.

[26]Murphy, A. B., and Arundell, C. J., "Transport Coefficient of Argon, Nitrogen, Oxygen, Argon–Nitrogen and Argon–Oxygen Plasmas," *Plasma Chemistry and Plasma Processing*, Vol. 14, No. 4, 1994, pp. 451–490.

K. Kailasanath
Associate Editor